Nano Research

Open Access

Research Article

High capacity and efficient dehydrogenation of aluminum hydride: Optimized by highly active TiN nanoparticles with low addition

Shaolei Zhao[1,2], Qingyun Shi[1,2], Long Liang[1,2], Chunmin Zhang[1,2], Qingshuang Wang[3], Chunli Wang[1] ✉, Ying Wang[1], Pai Huang[1] ✉, Limin Wang[1,2], and Yong Cheng[1] ✉

[1] *State Key Laboratory of Rare Earth Resource Utilization, Changchun Institute of Applied Chemistry, Chinese Academy of Sciences, Changchun 130022, China*
[2] *School of Applied Chemistry and Engineering, University of Science and Technology of China, Hefei 230026, China*
[3] *School of Materials Science and Engineering, Changchun University of Science and Technology, Changchun 130022, China*

Cite this article: *Nano Research*, **2025**, *18*, 94907318. https://doi.org/10.26599/NR.2025.94907318

ABSTRACT: Improving the dehydrogenation behavior of aluminum hydride (AlH_3) by introducing additives provides a promising avenue in portable hydrogen source applications. However, the challenge remains in the development of highly active additives that facilitate hydrogen storage in composites while maintaining high capacity with a relatively small amount of additive. This work presents the successful synthesis of TiN nanoparticles by nitriding reaction using TiO_2 as the precursor. The onset dehydrogenation temperature of AlH_3 could be remarkably reduced to 52.9 °C on account of the catalytic effect of TiN nanoparticles. Furthermore, the composite exhibits a close approximation to the realistic capacity of pure aluminum hydride, with a maximum capacity of 9.9 wt.%. The notable decrease in the apparent dehydrogenation activation energy of AlH_3 from 130.86 to 86.69 kJ·mol^{-1} after the incorporation of TiN substantiates the pivotal role of multivalent titanium and nitrogen.

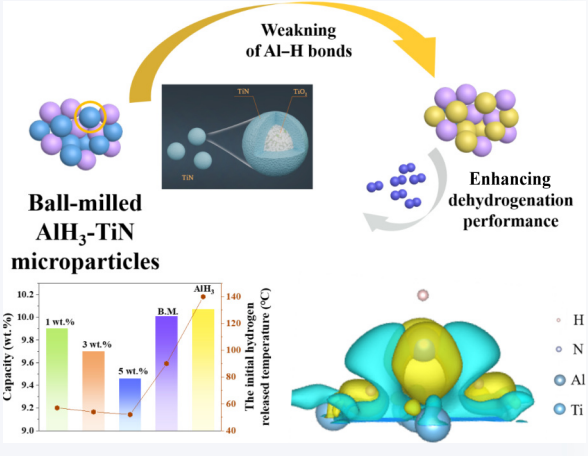

KEYWORDS: aluminum hydride, titanium nitride, high capacity, dehydrogenation, low addition

1 Introduction

With the deepening of research and development in low-cost transition metal catalysts and high-performance proton exchange membranes, hydrogen fuel cells have shown great potential for application, especially in terms of environmental friendliness that lithium-ion batteries cannot match. From the perspective of battery systems, efficient hydrogen supply is the key to ensuring the energy density of hydrogen fuel cells [1, 2]. Owing to the low dehydrogenation pressure, high product purity, and satisfactory safety, light metal hydrides have always been regarded as ideal solid hydrogen storage materials with considerable application prospects [3–7]. Aluminum hydride (AlH_3) plays an increasingly important role in lightweight mobile applications due to its ultra-high hydrogen storage capacity (10.1 wt.%, 148 kg·m^{-3} H_2) and relatively low dehydrogenation temperature (140 °C) among numerous light metal hydrides [8–11]. The present focus is on the practical application of aluminum hydride in the fuel cell-based hydrogen economy. Further improvement in its dehydrogenation temperature and kinetics is the following key step [12, 13]. Fortunately, it has been gradually discovered that developing efficient catalysts is of great significance in order to achieve kinetic/thermodynamic optimization in the field of catalytic dehydrogenation of light metal hydrides through continuous exploration [14–20]. Li et al. reported that under the catalysis of Ti_2C MXene, the onset hydrogen release temperature of magnesium hydride decreased by 37 °C [21]. He et al. designed a TiB_2 catalyzed aluminum hydride composite system, which could provide a capacity of 5.3 wt.% at 80 °C [22]. Our group constructed a AlH_3/MXene-supported PrF_3 nanosheets heterojunction, and the onset dehydrogenation temperature was dramatically decreased to 70.2 °C [23].

It can be concluded from the reported literatures that titanium-

Received: November 25, 2024; **Revised:** January 22, 2025
Accepted: February 21, 2025

✉Address correspondence to Chunli Wang, clwang@ciac.ac.cn; Pai Huang, Huangpai@ciac.ac.cn; Yong Cheng, cyong@ciac.ac.cn

based materials exhibit excellent modification effects on the dehydrogenation of aluminum hydride [24, 25]. Nevertheless, the cumbersome catalyst synthesis process and the scarcity of raw materials continue to impede the advancement of solid hydrogen storage. Furthermore, it should be noted that the capacity reduction caused by the large additive mass ratio and the uncontrollable ball milling process (B. M.) cannot be overlooked. The aforementioned issues serve to undermine the distinctive attributes of aluminum hydride, thus limiting its scope for application [26]. Consequently, the development of an easily prepared and hyperactive titanium-based catalyst, in conjunction with the design of a composite requiring minimal additive addition and ball milling time, represents a significant step towards the full potential of aluminum hydride [27, 28].

Herein, TiN nanoparticles synthesized by the high-temperature nitriding method were employed as efficient catalysts for promoting the dehydrogenation behavior of aluminum hydride. The catalytic activity of the nanoparticles is found to be satisfactory even at a trace amount of 1 wt.%. On that account, the composite demonstrates an excellent low-temperature dehydrogenation performance, exhibiting a capacity comparable to that of pure aluminum hydride. Concurrently, high catalytic activity allows for the hydrogen release to be completed within a relatively short period of time, effectively mitigating the uncontrollable capacity loss caused by the ball milling process. The combination of these two key factors provides the designed composite with a notable capacity advantage over previously published research in the field of aluminum hydride [29–32]. The results of the fitting indicate that the addition of additives can significantly reduce the energy barrier of dehydrogenation reaction. Moreover, a proposed catalytic mechanism based on density functional theory (DFT) calculations suggests alternative avenues for the design of nitrogen-containing catalysts with advantageous properties.

2 Experimental

2.1 Materials and equipment

All the chemical reagents and gas were commercially available and all the equipment undergone standard value correction. Anatase phase TiO_2 nanoparticles were produced by Rhawn Chemical Regent Co., Ltd. (Shanghai, China). The ammonia argon mixture was purchased from Dalian Special Gas Co., Ltd. (Dalian, China) and the volume ratio of argon to ammonia was 95:5. The α-AlH_3 powder was produced by Henan Nayu New Material Co., Ltd. (Henan, China). GSL-1500X vacuum tube furnace was purchased from Hefei Kejing Materials Technology Co., Ltd. (Hefei, China). QM-QX04 planetary ball mill and supporting stainless steel ball milling tank and ball milling beads were purchased from Nanda Instruments Co., Ltd. (Nanjing, China).

2.2 Synthesis

2.2.1 *Synthesis of TiN nanoparticles*

The TiO_2 precursor (0.12 g) was evenly laid in a porcelain crucible and placed in a vacuum tube furnace. The argon ammonia mixture was then injected into the vacuum tube furnace for 30 min at room temperature. Subsequently, once the atmosphere within the vacuum tube furnace was stabilized, the temperature should be slowly raised to 900 °C (2 °C·min^{-1} to 700 °C, then 1 °C·min^{-1} to 900 °C) and maintained for 1 h. Upon reaching room temperature naturally, black TiN nanoparticles could be collected and reserved.

2.2.2 *Synthesis of AlH_3-TiN composites*

The purchased α-AlH_3 powder was mixed with TiN nanoparticles in varying proportions (1 wt.%, 3 wt.%, and 5 wt.%), resulting in a total mass of 0.6 g. Thereafter, the powder mixture was placed in a stainless steel ball milling tank and milled at a ball-to-powder of 50 with a milling speed of 350 rpm for 60 min, which was named as TiN-0.01, TiN-0.03, and TiN-0.05, respectively. To prevent contamination from oxygen and moisture, the sample configuration, transfer, ball milling, and collection processes mentioned above were all carried out in an argon atmosphere.

2.3 Characterization

To analyze phase composition, X-ray diffraction (XRD) patterns were carried out through Bruker D8 Advance X diffractometer using Cu Kα radiation at a voltage of 40 kV and a current of 40 mA with a scan speed at 3.5 °·min^{-1}. Scanning electron microscopy (SEM, Hitachi S-4800 SEM analyzer) and transmission electron microscopy (TEM, FEI Tecnai G2 F20) were employed to further characterize the morphology and microstructure of the sample. Nitrogen isothermal adsorption curves were measured by Quantachrome AutoSorb-1 type physicochemical adsorption instrument. The element valence was explored by X-ray photoelectron spectroscopy (XPS, ESCALABM KII spectrometer) using Al Kα radiation with a wavelength of 8.53 Å as X-ray source. The dehydrogenation property and kinetics of different samples were tested using a Sievert style type instrument designed by Grinm Group Co., Ltd. and differential scanning calorimeter (DSC, METTLER TOLEDO DSC3) with a nitrogen flow at 60 mL·min^{-1}. The heating rate and cutoff temperature of the temperature controlled dehydrogenation (TPD) curves were 2 °C·min^{-1} and 250 °C, respectively. The heating rate from room temperature to the target temperature of thermostatic dehydrogenation was 4 °C·min^{-1}.

2.4 Calculation details

We calculated the electronic structures based on the DFT using the Vienna *ab initio* simulation package (VASP). The behavior of the core and electrons was described by the projector augmented wave (PAW) model with the Perdew–Burke–Ernzerhof (PBE) functional. The cutoff energy for the plane wave expansion of the electron wave function is set to 450 eV. The force and energy convergence criteria were set to 0.02 eV·Å^{-1} and 10^{-5} eV, respectively. Monkhorst–Pack *k*-points for all the calculations was applied of 3 × 3 × 1.

3 Results and discussion

3.1 Composition and morphology

The synthesis process and simplified structure diagram of nanoparticles are illustrated in Fig. 1(a). Combined with the XRD patterns, as shown in Fig. 1(b) and Fig. S1 in the Electronic Supplementary Material (ESM), it is known to all that the nitriding reaction first occurs on the surface of the precursor particles, generating titanium nitride crystals (JCPDS No. 38-1420). As the reaction proceeded, the outer layer of TiO_2 was almost completely converted into TiN crystals, preventing further nitriding of the core TiO_2. Thus, the core of precursor anatase TiO_2 (JCPDS No. 21-

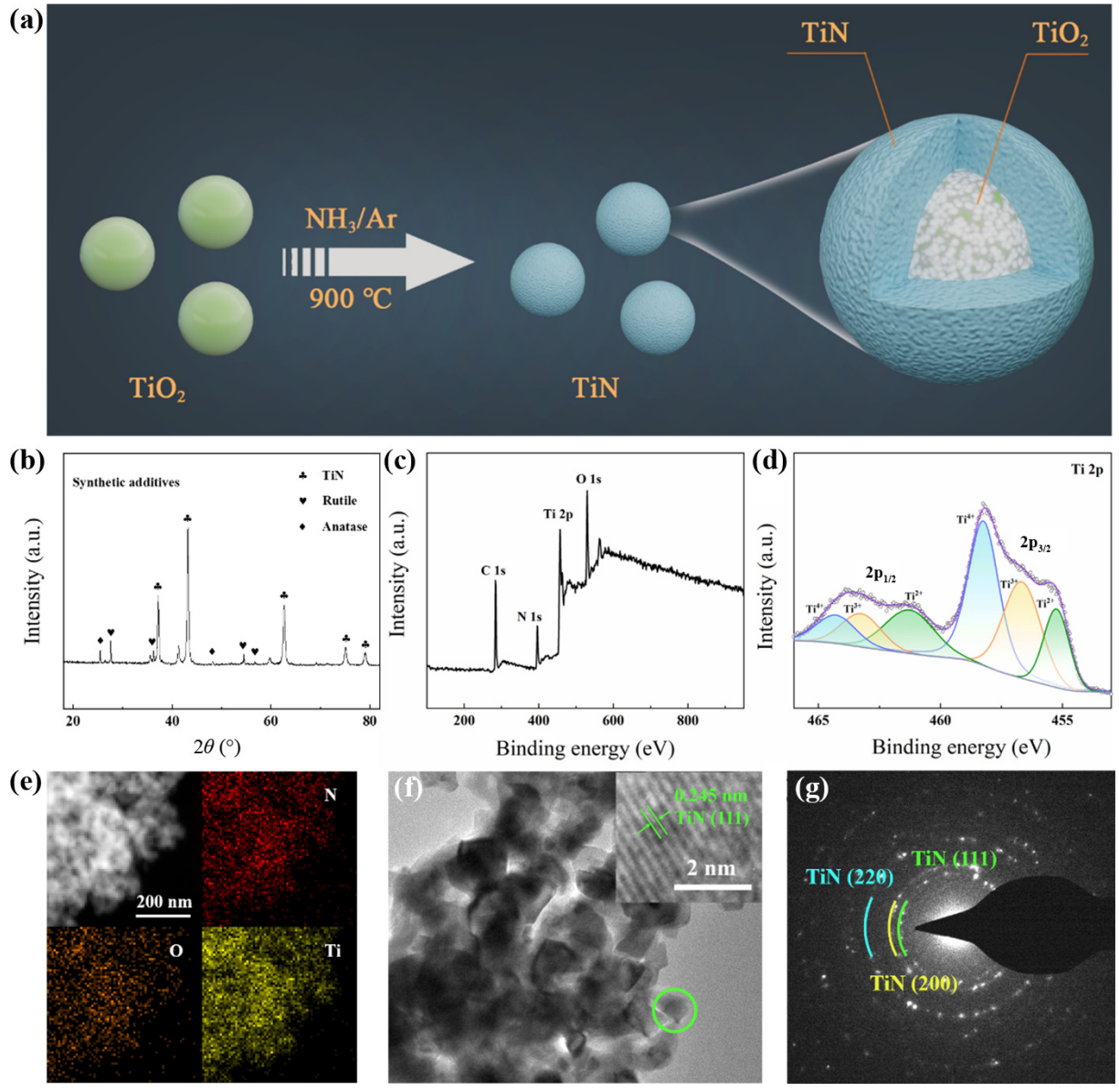

Figure 1 (a) Schematic diagram, (b) XRD pattern, (c) survey spectrum, (d) Ti 2p XPS spectrum, (e) elemental mappings, (f) TEM and HRTEM images, and (g) selected area electron diffraction results of synthesized TiN nanoparticles.

1272, XRD pattern is shown in Fig. S1 in the ESM) underwent a transformation to a more stable rutile phase (JCPDS No. 21-1276) at elevated temperature. Therefore, characteristic peaks of TiN, anatase TiO_2, and rutile TiO_2 can be simultaneously observed in the XRD pattern (Fig. 1(b)). Meanwhile, the XPS survey spectrum (Fig. 1(c)) demonstrates the presence of Ti, N, and O in the prepared TiN nanoparticles. Sharp peaks at binding energy of 455.3/461.5, 456.6/463.3, and 458.2/464.3 eV can be deconvoluted into $2p_{1/2}$–$2p_{3/2}$ spin-orbit doublets of Ti^{2+}, Ti^{3+}, and Ti^{4+}, respectively (Fig. 1(d)) [33]. Prior to the nitriding reaction, the majority of Ti existed in the form of Ti^{4+}, which indicated that several Ti^{4+} species were reduced to lower valence during the nitriding process due to the reducibility of ammonia and hydrogen produced by partial decomposition of ammonia. These results were consistent with those of similar synthesis methods previously reported [34]. From the element distribution mapping, as shown in Fig. 1(e), nitrogen is distributed evenly in the TiN nanoparticles, in accordance with the distribution of titanium element. Compared with the precursor, there was no discernible change in the crystal morphology or particle size before and after the nitriding reaction (Fig. S2 in the ESM). In addition, the exposed crystal planes with a clear lattice fringe of 0.245 nm were indexed into (111) plane of TiN nanoparticles, as can be seen from TEM and high-resolution TEM (HRTEM) images in Fig. 1(f) and Fig. S3 in the ESM. Furthermore, the characteristic diffraction rings of TiN crystal can also be observed in the selected area electron diffraction results (Fig. 1(g)). The aforementioned findings validated that titanium nitride nanoparticles were successfully synthesized via the ammonia nitriding reaction. It is also worth mentioning that the reason why the prepared nanoparticles are referred to as TiN particles in the article is that their main component in the catalytic reaction is the TiN component on the surface. The actual structure of the nanoparticles is shown in Fig. 1(a).

In order to investigate the modification effect of synthesized TiN nanoparticles, we prepared aluminum hydride composite materials by ball milling and designated them as TiN-0.01, TiN-0.03, and TiN-

0.05 according to the additive content. Based on SEM image in Fig. 2(a), a significantly reduced particle size can be observed in composites after ball milling in comparison to the as-received α-AlH_3. Meanwhile, the reduction in average particle diameter from 200 to 0.34 μm in TiN-0.05 contributed to the increased catalytic active sites, which facilitated the hydrogen transfer and desorption. It should be pointed out that the amount of additives added had no significant effect on particle size, as evidenced by the approximate distribution curves of other samples (Fig. S4 in the ESM). The elemental mapping results of TiN-0.05 in Fig. 2(b) manifest the uniform distribution of α-AlH_3 and TiN nanoparticles. It is evident from Fig. 2(c) that except for high-intensity characteristic peaks of α-AlH_3 (JCPDS No. 23-0761), the faintish diffraction peaks appearing at 36.7°, 42.6°, and 77.9° correspond to the crystal plane of TiN (111), (200), and (222), respectively. This indicated that during the ball milling process, neither the additive nor the aluminum hydride substrate underwent phase transition, simultaneously exhibiting the successfully mingle of α-AlH_3 and TiN particles. The nitrogen adsorption/desorption isotherms of TiN-0.05 at 77 K, as shown in Fig. 2(d), illuminate that composite exhibited a larger specific surface area of 21.04 $m^2 \cdot g^{-1}$ and wider average pore diameter of 3.10 nm, as compared to the as-received α-AlH_3 particles (3.80 $m^2 \cdot g^{-1}$, Fig. S6 in the ESM). The increased specific surface area also benefited from the reduced particle size, which was brought about by ball milling.

3.2 Dehydrogenation performance

To evaluate the dehydrogenation performance of composite, temperature-programmed hydrogen desorption (TPD) was employed to further analyze the dehydrogenation temperature and capacity (Fig. 3(a)) and the data of ball-milled and as-received α-AlH_3 were also listed for comparison. The corresponding differential curves of TPD curves in Fig. 3(b) reveal the peak dehydrogenation temperature of different composites to a certain extent. The maximum capacity amount was presented in ascending order as follows: TiN-0.05, TiN-0.03, TiN-0.01, ball-milled α-AlH_3, and as-received α-AlH_3 sample, with values of 9.46 wt.%, 9.70 wt.%, 9.89 wt.%, 10.01 wt.%, and 10.07 wt.%, respectively. On the basis of dehydrogenation capacity of the as-received α-AlH_3 sample, a calculation was performed to determine the theoretical capacity and capacity retentions, which could be utilized to assess the capacity loss caused by the ball milling process. From the capacity retention results, it was evident that an increase in additive content may also lead to a gradual increase in the capacity loss during ball milling. Nevertheless, the overall retention rate exceeded 98% for all composites. On the contrary, as the addition amount increased, the onset dehydrogenation temperature continuously decreased, which was more conducive to the continuous supply of hydrogen to the composite at lower temperatures. The onset dehydrogenation temperatures of samples TiN-0.01, TiN-0.03, and TiN-0.05 were found to be 56.8, 54.5, and 52.9 °C, representing a reduction in the

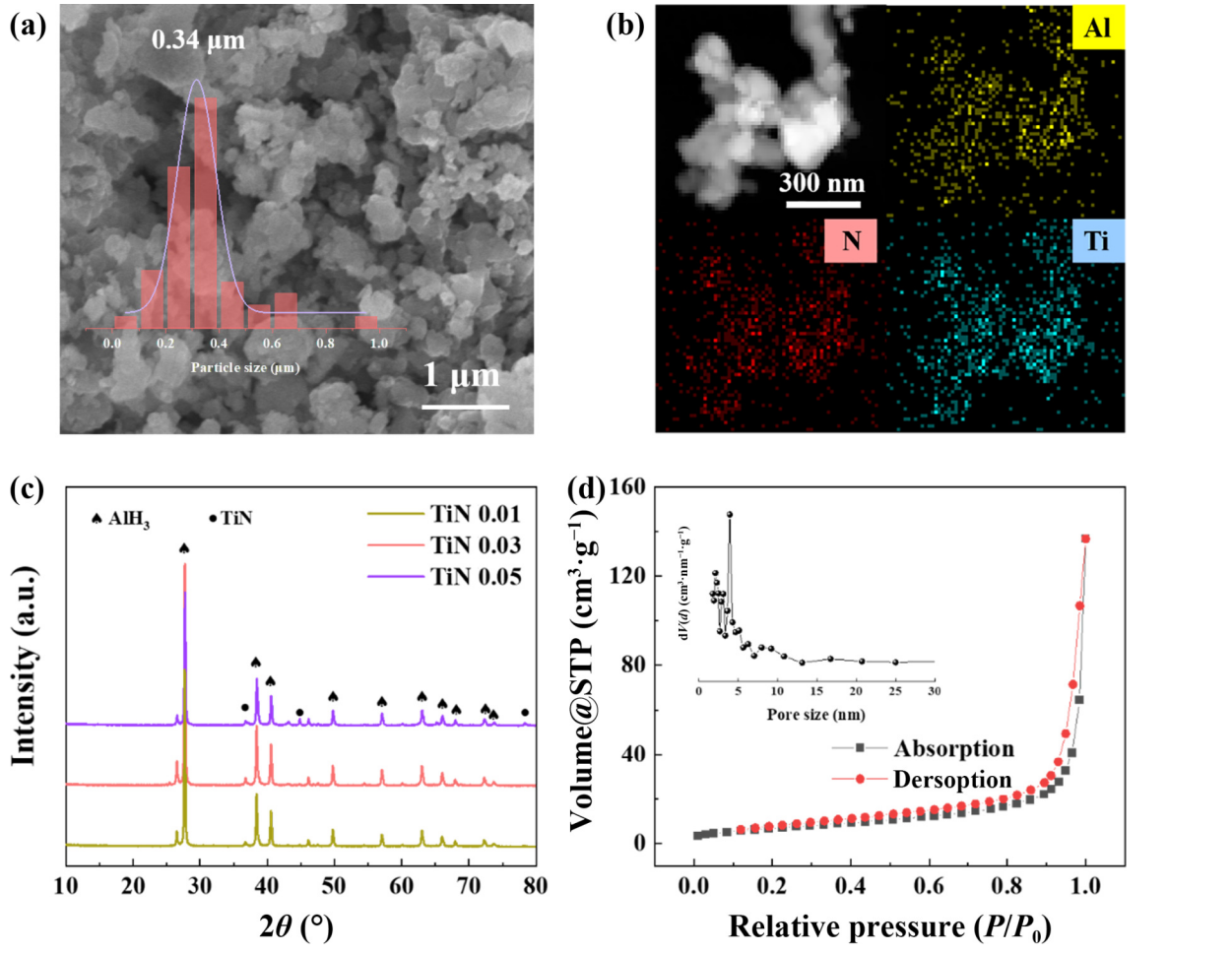

Figure 2 (a) SEM image and particle size distribution curve, (b) elements mapping images of TiN-0.05, (c) XRD patterns of different samples, and (d) nitrogen adsorption/desorption curves and pore size distribution of TiN-0.05.

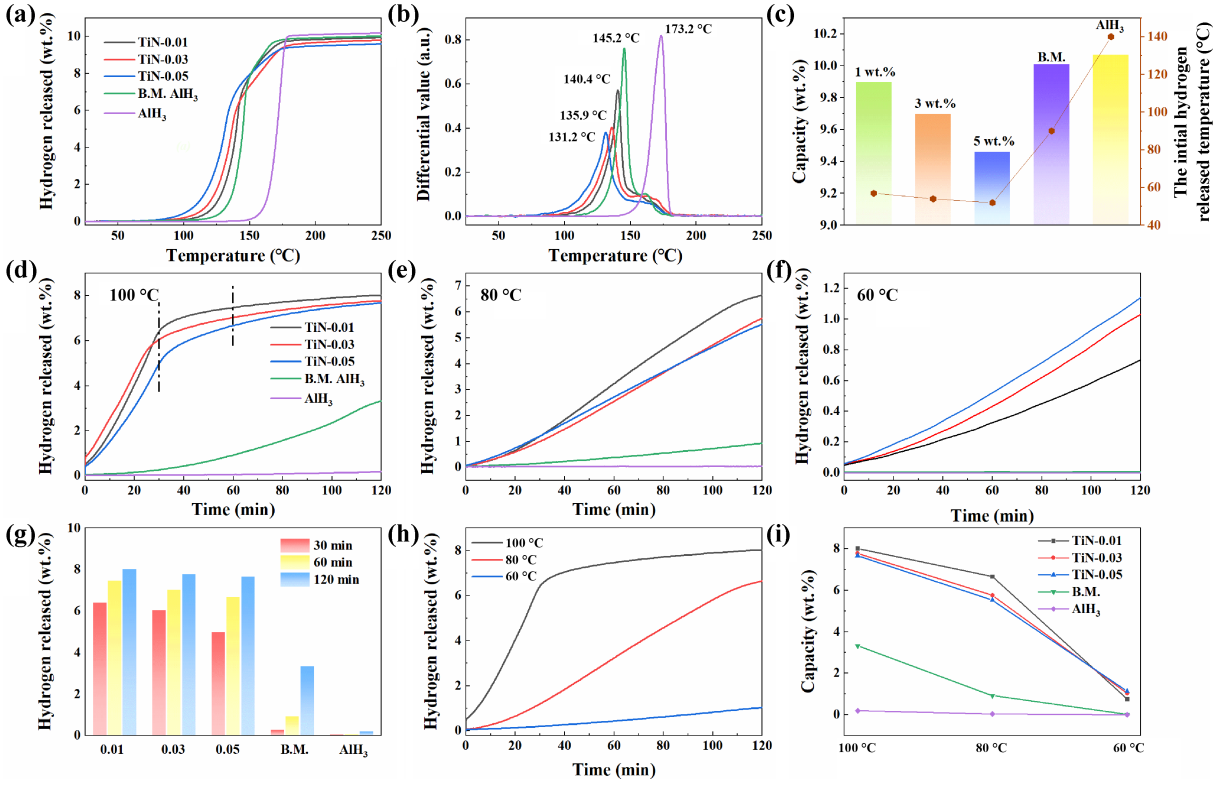

Figure 3 (a) TPD curves, (b) differential curves of TPD curves, (c) capacity and onset dehydrogenation temperature, ((d)–(f)) 100, 80, and 60 °C thermostatic dehydrogenation curves, (g) hydrogen released capacity under 100 °C of all samples, (h) thermostatic dehydrogenation curves of sample TiN-0.01 under different temperature, and (i) the relationship between hydrogen released capacity and dehydrogenation temperature.

Table 1 Summary of TPD results

Sample	Onset dehydrogenation temperature (°C)	Capacity (wt.%)	Theoretical capacity (wt.%)	Retention (%)
TiN-0.01	56.8	9.89	9.97	99.2
TiN-0.03	54.5	9.70	9.77	99.3
TiN-0.05	52.9	9.46	9.57	98.8
B. M. α-AlH_3	90.1	10.01	10.07	99.4
α-AlH_3	140.0	10.07	—	—

ratio by 59.4%, 61.1%, and 62.2%, compared with the as-received α-AlH_3 sampler. However, the decrease in temperature was not as pronounced as that in capacity and raised confusion about the overall effectiveness of the approach. Figure 3(c) and Table 1 summarize the TPD data. Furthermore, in order to investigate the dehydrogenation behavior of composite at low temperatures, a series of composites were subjected to thermostatic dehydration under 100, 80, and 60 °C (Figs. 3(d)–3(f)). Obviously, when the temperature was above 80 °C, the hydrogen desorption kinetic of TiN-0.01 composite was optimal, capable of releasing 6.41 wt.%, 7.46 wt.%, and 8.02 wt.% hydrogen within the first 30, 60, and 120 min at 100 °C. Moreover, the hydrogen release for 2 h reached 81% of the total capacity. Under the same circumstances, ball-milled α-AlH_3 was observed merely release 0.25 wt.%, 0.87 wt.%, and 3.12 wt.% hydrogen, while the as-received α-AlH_3 exhibited negligible hydrogen desorption. Figure 3(g) and Table S1 in the ESM illustrate the histogram of dehydrogenation amount versus time under 100 °C. The incorporation of TiN additives effectively improved the dehydrogenation kinetics of aluminum hydrides, and was significantly more efficient than the approach of achieving nano-materialization solely through ball milling. Furthermore, when the temperature dropped to 80 °C, the effective dehydrogenation amount of TiN-0.01 could still reach up to 6.66 wt.% within 2 h, whereas the ball-milled α-AlH_3 was severely limited to 0.83 wt.% (Fig. 3(e) and Table S2 in the ESM). However, when the temperature further was further reduced to 60 °C, aluminum hydride without TiN addition no longer underwent a dehydrogenation reaction, and TiN-0.05 instead provided the maximum dehydrogenation amount of 1.14 wt.% within 2 h. The capacity of TiN-0.01 composite within 2 h was only 0.74 wt.% (Fig. 3(f) and Table S3 in the ESM), which was likely due to the fact that at relatively low temperature, only the fully weakened Al–H bond could be broken. Besides, the proportion of fully weakened Al–H bonds increased in direct correlation with the concentration of additives when the content fell below a specified threshold level. This phenomenon was consistent with the test results of numerous reported works currently available. Figure 3(h) shows the thermostatic dehydrogenation curves of sample TiN-0.01 under different temperature. Figure 3(i) depicts the trend of dehydrogenation capacity in 2 h as a function of temperature for a series of composites. Contrary to ball-milled α-AlH_3, composites containing TiN additives exhibited much smaller attenuation amplitudes from 100 to 80 °C in terms of dehydrogenation kinetics and available capacity compared to those from 80 to 60 °C. This implied that the capacity and kinetics of the composite could be fully guaranteed within the operational temperature range of the fuel cell (80 °C), which represented an extremely beneficial property for the development of hydrogen storage tank-fuel cell hybrid devices. As shown in Table S4 in the ESM, the improvement of dehydrogenation kinetics of additives in this work is progressiveness compared with other work in this field.

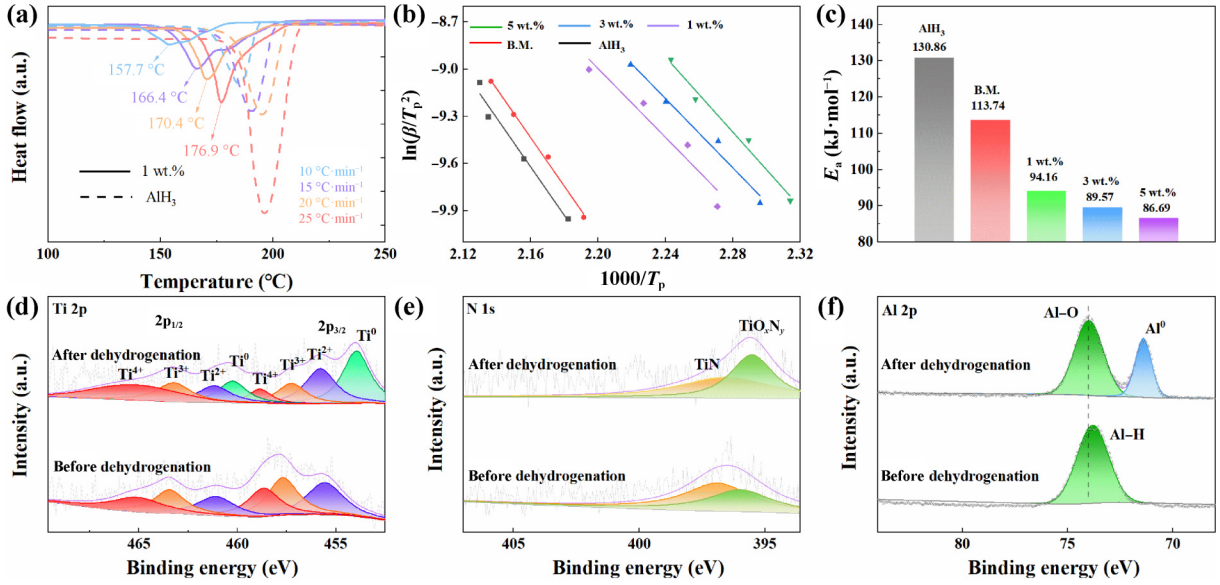

Figure 4 (a) DSC curves of TiN-0.01 and as-received α-AlH_3 of different heat rates, (b) the Kissinger's plot, and (c) the activation energy of dehydrogenation reaction of all the samples. (d) Ti 2p, (e) N 1s, and (f) Al 2p XPS spectra of TiN-0.05 before and after dehydrogenation.

Figure 4(a) and Fig. S7 in the ESM show the DSC curves of different composites, where the sharp endothermic peak corresponded to the process of thermal decomposition of aluminum hydride to generate metallic aluminum and H_2. It was obvious that compared to the as-received aluminum hydride, the peak temperature of the endothermic peak was lower in the presence of TiN additive under the same heating rate. This result was consistent with the TPD curves and differential curves, once again confirming that the addition of TiN nanoparticles could effectively reduce the dehydrogenation temperature of aluminum hydride. Meanwhile, the apparent activation energy (E_a) of dehydrogenation reaction was calculated by the Kissinger equation based on the DSC test results

$$\ln\frac{\beta}{T_p^2} = -\frac{E_a}{RT_p} + \ln\frac{AR}{E_a} \quad (1)$$

where β, T_p, E_a, A, and R indicate the heating rate, the temperature at the peak reaction rate, the apparent activation energy, a constant factor, and gas constant, respectively. The apparent activation energy of TiN-0.05 was the smallest (86.69 kJ·mol^{-1}), with a decrease of 33.8% and 23.8% compared to the as-received α-AlH_3 (130.86 kJ·mol^{-1}) and ball-milled α-AlH_3 (113.74 kJ·mol^{-1}), respectively (Figs. 4(b) and 4(c)). The reduction in apparent activation energy resulting from the addition of additives was the fundamental factor responsible for the enhancement of low-temperature dehydrogenation kinetics. Furthermore, in order to investigate the mechanism of TiN nanoparticles optimization effect in dehydrogenation process, XPS was employed to figure out the chemical state differences before and after dehydrogenation. Figures 4(d)–4(f) show the Ti 2p, N 1s, and Al 2p XPS spectra in TiN-0.05 composite. As illustrated in Fig. 4(d), the peaks at binding energy of 454.0/460.2 eV can be ascribed to $2p_{1/2}$–$2p_{3/2}$ spin-orbit doublets of Ti^0, which cannot be observed before dehydrogenation. And the ratio of Ti^0, Ti^{2+}, Ti^{3+}, and Ti^{4+} has undergone a notable transformation from 0:1.13:1.2:1 to 1.7:1.3:1:1, suggesting a decline in $Ti^{3+}$and Ti^{4+} and an increase in Ti^0 and Ti^{2+}. This phenomenon could be explained by the oxidized Ti atoms on the surface of the additive, which were reduced by the negatively charged H ions. The electron withdrawing properties of Ti atoms exhibited during electron transfer facilitated the removal of H^- [35]. In the meantime, the ratio of nitrogen in TiN to that in TiO_xN_y has changed from 0.87 to 1.09 (Fig. 4(e)). This may be attributed to the fact that nitrogen acted as a bridge, participating in the electron transfer between the inner layer and surface layer Ti atoms, which further increased the amount of Ti atoms with catalytic activity [36]. These results indicated that TiN nanoparticles were of great significance in improving the dehydrogenation behavior of aluminum hydride. Besides, as shown in Fig. 4(f), aluminum after dehydrogenation mainly exists in the metallic state with minor oxidation state resulting from partial oxidation during the testing process. This proved a lack of chemical reaction between aluminum hydride and TiN nanoparticles in the dehydrogenation reaction.

3.3 Mechanism exploration

To elucidate the catalytic mechanism of TiN nanoparticles, further exploration was conducted based on DFT to simulate the charge density and changes in Al–H bonds. Based on the analyses of XRD and TEM results, we chose the (111) plane of TiN as the targeted location for the adsorption of α-AlH_3 molecules (Fig. 5(a)). The bond lengths of Al–H1, Al–H2, and Al–H3 in aluminum hydride molecules adsorbed on the surface of additives were 1.593, 2.192, and 2.255 Å, which gave an average growth of 0.421 Å compared to that of α-AlH_3 molecules (1.592 Å). Figure 5(b) shows the charge density difference of the AlH_3-TiN model. Obviously, there was a significant electron enrichment between Al–H2 and Al–H3, which signified that the negatively charged hydrogen exhibited enhanced reducibility. Consequently, the strength of Al–H bonds was weakened to some extent. The partial density of states (PDOS, Fig. 5(c)) also corroborates this result, demonstrating weakened bonding strengths of *s*(H) and *s*(Al) at the Fermi level.

Based on the above test results and analysis, we proposed a possible catalytic mechanism. The role of metal active sites mainly consists of two parts. One is to provide adsorption active sites for aluminum hydride analysis. Because based on the energy simulation of the theoretical calculation modeling process, we found that aluminum hydride molecules tend to adsorb more on the surface of Ti atoms. The second is that Ti, as a hydrogen absorbing element, has affinity for active hydrogen and can

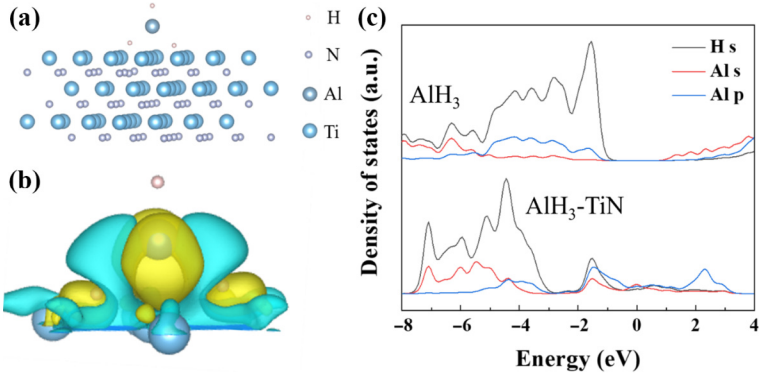

Figure 5 (a) Structure and (b) charge density difference of the AlH_3-TiN model and (c) PDOS of pure AlH_3 and AlH_3-TiN.

promote hydrogen transport and desorption. When the transmission of hydrogen accelerates, the limitations on metal nucleation are weakened, and active metal nuclei are more easily formed, which can effectively improve the efficiency of its self-catalytic reaction and thus enhance its kinetics. On the other hand, the main function of nitrogen is to weaken the hydrogen aluminum bond. Due to the electron withdrawing property of nitrogen itself, the interaction between negatively charged hydrogen in adsorbed aluminum hydride molecules causes the electron pairs to shift towards hydrogen, weakening the Al–H bond and reducing the energy required for bond breaking. This phenomenon is often mentioned in existing research on metal hydrides. In addition, non-metallic elements also play a bridging role in electron transfer, which is very common in many chemical reactions.

In summary, the synergistic effect between metals and non-metals significantly optimizes the dissociation, diffusion, binding, and desorption processes of active hydrogen, thereby enabling the dehydrogenation reaction to exhibit more excellent kinetics. This synergy ensured that the additive could also achieve satisfactory modification effect even at low dosage.

4 Conclusion

In summary, the synthesis of TiN-AlH_3 composite through ball milling resulted in the change in the bonding state of H and Al, which in turn caused a decrease in the initial hydrogen release temperature of the composite to 52.9 °C. Due to the extremely low dosage of additives allowed the composite to reach a maximum capacity of 9.89 wt.%. At the same time, the dehydrogenation reaction kinetics in the low-temperature region have also been significantly improved. TiN-0.01 could release 8.02 wt.% hydrogen within 2 h at 100 °C and TiN-0.05 can release over 1 wt.% hydrogen within 2 h at 60 °C. The apparent activation energy of the dehydrogenation reaction of the composite sample was only 86.69 kJ·mol^{-1}, representing a 33.8% reduction compared to the as-received α-AlH_3. The synergistic effect between Ti and N during electron transfer was considered the main source of catalytic activity based on density functional theory.

Electronic Supplementary Material: Supplementary material (XRD pattern of TiO_2 precursor; SEM images of TiO_2 and TiN nanoparticles; HRTEM images of TiN nanoparticles; SEM images and particle size distribution curve of TiN-0.01 and TiN-0.03; SEM images of as-received α-AlH_3; nitrogen adsorption/desorption curves and pore size distribution of as-received α-AlH_3; summary table of the relationship between constant temperature dehydrogenation amount and time under 100, 80, and 60 °C of different samples; and DSC curves of ball-milled AlH_3, TiN-0.03, and TiN-0.05 under different heat rates) is available in the online version of this article at https://doi.org/10.26599/NR.2025.94907318.

Data availability

All data needed to support the conclusions in the paper are presented in the manuscript and the Electronic Supplementary Material. Additional data related to this paper may be requested from the corresponding author upon request.

Acknowledgements

The authors acknowledged the National Key Research and Development Program of China (No. 2021YFB4000604), Special fund of Scientific and Technological Cooperation Program between Jilin Province and Chinese Academy of Sciences (No. 2024SYHZ0030), Jilin Provincial Scientific and Technological Development Program (Nos. 20200401039GX, 2022021109GX, 20230201140GX, and 20230201125GX), Tianjin Scientific and Technological Plan Project (No. 23YFYSHZ00260), Youth Innovation Promotion Association CAS (No. 2021225), and Youth Growth Science and Technology Program of Jilin Province (No. 20220508001RC).

Declaration of competing interest

All the contributing authors report no conflict of interests in this work.

Author contribution statement

S. L. Z.: Data curation, formal analysis, investigation, methodology, writing – original. Q. Y. S.: Writing – review & editing. L. L.: Investigation, validation. C. M. Z.: Resources. Q. S. W.: Funding acquisition. C. L. W.: Data curation. Y. W.: Software. P. H.: Funding acquisition. L. M. W.: Writing – review & editing. Y. C.: Funding acquisition, supervision. All the authors have approved the final manuscript.

Use of AI statement

None.

References

[1] Olabi, A. G.; Sayed, E. T. Developments in hydrogen fuel cells. *Energies* **2023**, *16*, 2431.
[2] Gitushi, K. M.; Blaylock, M. L.; Klebanoff, L. E. Hydrogen gas

dispersion studies for hydrogen fuel cell vessels II: Fuel cell room releases and the influence of ventilation. *Int. J. Hydrogen Energy* **2022**, *47*, 21492–21505.
[3] Ouyang, L. Z.; Jiang, J.; Chen, K.; Zhu, M.; Liu, Z. W. Hydrogen production via hydrolysis and alcoholysis of light metal-based materials: A review. *Nano-Micro Lett.* **2021**, *13*, 134.
[4] Drawer, C.; Lange, J.; Kaltschmitt, M. Metal hydrides for hydrogen storage—Identification and evaluation of stationary and transportation applications. *J. Energy Storage* **2024**, *77*, 109988.
[5] Wang, Y. T.; Xue, Y. D.; Züttel, A. Nanoscale engineering of solid-state materials for boosting hydrogen storage. *Chem. Soc. Rev.* **2024**, *53*, 972–1003.
[6] Yan, S.; Wei, L. J.; Gong, Y.; Yang, K. Enhanced hydrogen storage properties of magnesium hydride by multifunctional carbon-based materials: A review. *Int. J. Hydrogen Energy* **2024**, *55*, 521–541.
[7] Ren, L.; Li, Y. H.; Zhang, N.; Li, Z.; Lin, X.; Zhu, W.; Lu, C.; Ding, W. J.; Zou, J. X. Nanostructuring of Mg-based hydrogen storage materials: Recent advances for promoting key applications. *Nano-Micro Lett.* **2023**, *15*, 93.
[8] Jiang, W.; Wang, H.; Zhu, M. AlH_3 as a hydrogen storage material: Recent advances, prospects and challenges. *Rare Met.* **2021**, *40*, 3337–3356.
[9] Nakagawa, Y.; Isobe, S.; Wang, Y. M.; Hashimoto, N.; Ohnuki, S.; Zeng, L.; Liu, S. S.; Ichikawa, T.; Kojima, Y. Dehydrogenation process of AlH_3 observed by TEM. *J. Alloys Compd.* **2013**, *580*, S163–S166.
[10] Yu, M. H.; Zhu, Z. Y.; Li, H. P.; Yan, Q. L. Advanced preparation and processing techniques for high energy fuel AlH_3. *Chem. Eng. J.* **2021**, *421*, 129753.
[11] Liu, H. Z.; Zhang, L. F.; Ma, H. Y.; Lu, C. L.; Luo, H.; Wang, X. H.; Huang, X. T.; Lan, Z. Q.; Guo, J. Aluminum hydride for solid-state hydrogen storage: Structure, synthesis, thermodynamics, kinetics, and regeneration. *J. Energy Chem.* **2021**, *52*, 428–440.
[12] Deng, J. F.; Sun, B. X.; Xu, J. R.; Shi, Y.; Xie, L.; Zheng, J.; Li, X. G. A monolithic sponge catalyst for hydrogen generation from sodium borohydride solution for portable fuel cells. *Inorg. Chem. Front.* **2021**, *8*, 35–40.
[13] Pramuanjaroenkij, A.; Kakaç, S. The fuel cell electric vehicles: The highlight review. *Int. J. Hydrogen Energy* **2023**, *48*, 9401–9425.
[14] Netskina, O. V.; Tayban, E. S.; Ozerova, A. M.; Komova, O. V.; Simagina, V. I. Solid-state $NaBH_4$/Co composite as hydrogen storage material: Effect of the pressing pressure on hydrogen generation rate. *Energies* **2019**, *12*, 1184.
[15] Yusnizam, N. Y.; Ali, N. A.; Sazelee, N. A.; Nasef, M. M.; Jalil, A. A.; Ismail, M. Boosting the de-/rehydrogenation properties of MgH_2 with the addition of $BaCoF_4$. *J. Alloys Compd.* **2023**, *967*, 171618.
[16] Pratthana, C.; Yang, Y. W.; Rawal, A.; Aguey-Zinsou, K. F. Nanoconfinement of lithium alanate for hydrogen storage. *J. Alloys Compd.* **2022**, *926*, 166834.
[17] Lan, Z. Q.; Fu, H.; Zhao, R. L.; Liu, H. Z.; Zhou, W. Z.; Ning, H.; Guo, J. Roles of *in situ*-formed NbN and Nb_2O_5 from N-doped Nb_2C MXene in regulating the re/hydrogenation and cycling performance of magnesium hydride. *Chem. Eng. J.* **2022**, *431*, 133985.
[18] Ren, Z. H.; Zhang, X.; Huang, Z. G.; Hu, J. J.; Li, Y. Z.; Zheng, S. Y.; Gao, M. X.; Pan, H. G.; Liu, Y. F. Controllable synthesis of 2D TiH_2 nanoflakes with superior catalytic activity for low-temperature hydrogen cycling of $NaAlH_4$. *Chem. Eng. J.* **2022**, *427*, 131546.
[19] Zhang, X. Y.; Sun, Y. H.; Ju, S. L.; Ye, J. K.; Hu, X. C.; Chen, W.; Yao, L.; Xia, G. L.; Fang, F.; Sun, D. L. et al. Solar‐driven reversible hydrogen storage. *Adv. Mater.* **2023**, *35*, 2206946.
[20] Wei, S.; Liu, J. X.; Xia, Y. P.; Zhang, H. Z.; Cheng, R. G.; Sun, L. X.; Xu, F.; Bu, Y. T.; Liu, Z. Y.; Huang, P. R. et al. Enhanced hydrogen storage properties of $LiAlH_4$ by excellent catalytic activity of $XTiO_3$@h‐BN (X = Co, Ni). *Adv. Funct. Mater.* **2022**, *32*, 2110180.
[21] Li, J. X.; Wang, S.; Du, Y. L.; Liao, W. H. Catalytic effect of Ti_2C MXene on the dehydrogenation of MgH_2. *Int. J. Hydrogen Energy* **2019**, *44*, 6787–6794.
[22] He, S. X.; Li, G. X.; Wang, Y.; Liu, L.; Lu, Z. Q.; Xu, L.; Sheng, P.; Wang, X. H.; Chen, H. Q.; Huang, C. K. et al. Achieving both high hydrogen capacity and low decomposition temperature of the metastable AlH_3 by proper ball milling with TiB_2. *Int. J. Hydrogen Energy* **2023**, *48*, 3541–3551.
[23] Liang, L.; Zhao, S. L.; Wang, C. L.; Yin, D. M.; Wang, S. H.; Wang, Q. S.; Liang, F.; Li, S. L.; Wang, L. M.; Cheng, Y. Heterojunction synergistic catalysis of MXene-supported PrF_3 nanosheets for the efficient hydrogen storage of AlH_3. *Nano Res.* **2023**, *16*, 9546–9552.
[24] Kong, Q. Q.; Zhang, H. H.; Yuan, Z. L.; Liu, J. M.; Li, L. X.; Fan, Y. P.; Fan, G. X.; Liu, B. Z. *Hamamelis*-like $K_2Ti_6O_{13}$ synthesized by alkali treatment of Ti_3C_2 MXene: Catalysis for hydrogen storage in MgH_2. *ACS Sustainable Chem. Eng.* **2020**, *8*, 4755–4763.
[25] Liang, L.; Zhang, C. M.; Zhao, S. L.; Liu, B. Z.; Wang, L. M.; Liang, F. Platinum-functionalized MXene serving as electron transport layer for highly efficiently catalyze dehydrogenation of AlH_3 with capacity of 9.3 wt.%. *Chem. Eng. J.* **2023**, *451*, 138791.
[26] Zhao, L.; Xu, F.; Zhang, C. C.; Wang, Z. Y.; Ju, H. Y.; Gao, X.; Zhang, X. X.; Sun, L. X.; Liu, Z. W. Enhanced hydrogen storage of alanates: Recent progress and future perspectives. *Prog. Nat. Sci.: Mater. Int.* **2021**, *31*, 165–179.
[27] Liang, L.; Wang, C. L.; Ren, M. G.; Li, S. L.; Wu, Z. J.; Wang, L. M.; Liang, F. Unraveling the synergistic catalytic effects of TiO_2 and Pr_6O_{11} on superior dehydrogenation performances of α-AlH_3. *ACS Appl. Mater. Interfaces* **2021**, *13*, 26998–27005.
[28] Gao, H. G.; Shao, Y. T.; Shi, R.; Liu, Y. N.; Zhu, J. L.; Liu, J. C.; Zhu, Y. F.; Zhang, J. G.; Li, L. Q.; Hu, X. H. Effect of few-layer $Ti_3C_2T_x$ supported nano-Ni via self-assembly reduction on hydrogen storage performance of MgH_2. *ACS Appl. Mater. Interfaces* **2020**, *12*, 47684–47694.
[29] Nakagawa, Y.; Lee, C. H.; Matsui, K.; Kousaka, K.; Isobe, S.; Hashimoto, N.; Yamaguchi, S.; Miyaoka, H.; Ichikawa, T.; Kojima, Y. Doping effect of Nb species on hydrogen desorption properties of AlH_3. *J. Alloys Compd.* **2018**, *734*, 55–59.
[30] Duan, C. W.; Cao, Y. Z.; Hu, L. X.; Fu, D.; Ma, J. L.; Youngblood, J. An efficient mechanochemical synthesis of alpha-aluminum hydride: Synergistic effect of TiF_3 on the crystallization rate and selective formation of alpha-aluminum hydride polymorph. *J. Hazard. Mater.* **2019**, *373*, 141–151.
[31] Yang, J. X.; Liang, F.; Cheng, Y.; Yin, D. M.; Wang, L. M. Improvement of dehydrogenation performance by adding CeO_2 to α-AlH_3. *Int. J. Hydrogen Energy* **2020**, *45*, 2119–2126.
[32] Liang, L.; Yang, Q. Q.; Zhao, S. L.; Wang, L. M.; Liang, F. Excellent catalytic effect of $LaNi_5$ on hydrogen storage properties for aluminium hydride at mild temperature. *Int. J. Hydrogen Energy* **2021**, *46*, 38733–38740.
[33] Mangolini, L.; Thimsen, E.; Kortshagen, U. High-yield plasma synthesis of luminescent silicon nanocrystals. *Nano Lett.* **2005**, *5*, 655–659.
[34] Schramke, K. S.; Qin, Y. X.; Held, J. T.; Mkhoyan, K. A.; Kortshagen, U. R. Nonthermal plasma synthesis of titanium nitride nanocrystals with plasmon resonances at near-infrared wavelengths relevant to photothermal therapy. *ACS Appl. Nano Mater.* **2018**, *1*, 2869–2876.
[35] Shi, Q. Y.; Gao, Y. X.; Zhao, S. L.; Zhang, C. M.; Liu, C.; Wang, C. L.; Wang, S. H.; Li, Y. Z.; Yin, D. M.; Wang, L. M. et al. Interfacial engineering of fluorinated TiO_2 nanosheets with abundant oxygen vacancies for boosting the hydrogen storage performance of MgH_2. *Small* **2024**, *20*, 2307965.
[36] Konashuk, A. S.; Filatova, E. O.; Sakhonenkov, S. S.; Kolomiiets, N. M.; Afanas'ev, V. V. Analysis of oxygen and nitrogen redistribution at interfaces of HfO_2 with laminate TiN/TiAl/TiN electrodes. *J. Phys. Chem. C* **2020**, *124*, 16171–16176.